AIAA 2001–2630

2-D/Axisymmetric Formulation of Multi-dimensional Upwind Scheme

William A. Wood and William L. Kleb
NASA Langley Research Center, Hampton, VA 23681

15th AIAA Computational Fluid Dynamics Conference
June 11–14, 2001
Anaheim, CA

2-D/Axisymmetric Formulation of Multi-dimensional Upwind Scheme

William A. Wood* and William L. Kleb*

NASA Langley Research Center, Hampton, VA 23681

A multi-dimensional upwind discretization of the two-dimensional/axisymmetric Navier-Stokes equations is detailed for unstructured meshes. The algorithm is an extension of the fluctuation splitting scheme of Sidilkover. Boundary conditions are implemented weakly so that all nodes are updated using the base scheme, and eigen-value limiting is incorporated to suppress expansion shocks. Test cases for Mach numbers ranging from 0.1–17 are considered, with results compared against an unstructured upwind finite volume scheme. The fluctuation splitting inviscid distribution requires fewer operations than the finite volume routine, and is seen to produce less artificial dissipation, leading to generally improved solution accuracy.

Nomenclature

A	Flux Jacobian
$\mathcal{A}$	Auxiliary variables flux Jacobian
B	Axisymmetric source term
C_f	Skin friction coefficient
C_p	Pressure coefficient
D	Linearity preserving matrix
E	Total energy
F	Flux function
H	Total Enthalpy
M	Upwinding matrix
P	Pressure
Q	Limiter ratio
R	Gas constant
R_e	Reynolds' number
S	Area
T	Temperature
U	Conserved variables
V	Primitive variables
$\mathcal{V}$	Projected velocity
W	Auxiliary variables
X	Eigen-vectors
$\mathcal{X}$	Auxiliary variables eigen-vectors
Z	Parameter vector
a	Sound speed
c_p	Specific heat
e	Internal energy
ℓ	Length
n, t	Normal/tangential vectors
q	Heat-transfer rate
r	Position vector
t	Time
u, v	Velocity components
x, y	Cartesian coordinates
Γ	Generalized integration surface
Λ	Eigen-values
Ω	Generalized integration volume
Φ	Finite volume artificial dissipation
α, β	Curvilinear advection speeds
δ	Incremental amount
γ	Ratio of specific heats
κ	Thermal conductivity
μ	Coefficient of viscosity
ϕ	Fluctuation
ψ	Limiter function
ρ	Density
τ	Shear stress
υ	Finite element shape function
ϖ	Axisymmetric switch
ξ, η	Curvilinear coordinates

Superscripts:

^{i}	Inviscid
^{v}	Viscous
$^\mathsf{T}$	Transpose
$^{x,y,\xi,\eta}$	Spatial component of a vector
*	Second-order fluctuation
$^\prime$	Fluctuation splitting artificial dissipation

Subscripts:

$_0$	Current node
$_\infty$	Freestream
$_o$	Stagnation value
$_w$	Wall
$_{\mathsf{R,L}}$	Right/left
$_\mathsf{T}$	Triangle
$_{i,j,k}$	Indicies

*Aerospace Engineer, Aerothermodynamics Branch, Aerodynamics, Aerothermodynamics, & Acoustics Competency.

Notation:

AOA	Angle of attack
COE	Contributions from other elements
LHS	Left-hand side
RHS	Right-hand side
∇	Gradient
Δ	Backward difference
ϵ	Permutation operator

Bold indicates vectors of the system of equations. The vector symbol, $\vec{}$, indicates spatial vectors. Tilde quantities are Roe-averaged, while the overbar is for linearly averaged quantities. Hats denote unit vectors. The breve symbol, $\breve{}$, indicates quantities in auxiliary variables. Subscripts of other variables indicate differentiation.

Introduction

UPWIND fluctuation splitting and finite volume discretization schemes are detailed for the two-dimensional and axisymmetric equations of motion for a perfect gas on triangulated domains. Both the finite volume and fluctuation splitting upwind schemes are applied to the inviscid flux, while the viscous flux is discretized with a scheme analogous to finite element.

Verification and validation of the schemes is performed using the test cases and methodology of Shinghal[1] and Roache,[2] with examples ranging from the incompressible flat plate to a Mach-17 cylinder.

New contributions include the axisymmetric formulation of the upwind fluctuation splitting distribution, the proper form for eigen-value limiting for this scheme, the head-to-head comparison of finite volume and fluctuation splitting, and the application of fluctuation splitting to a hypersonic heat-transfer validation test.

Formulations

The Navier[3]-Stokes[4] system of equations can be written in two-dimensional or axisymmetric non-dimensional form as,

$$\varpi_a \mathbf{U}_t + \vec{\nabla}\cdot(\varpi_a \vec{\mathbf{F}}^i) = \vec{\nabla}\cdot(\varpi_a \vec{\mathbf{F}}^v) + \varpi \mathbf{B}^i - \varpi \mathbf{B}^v \quad (1)$$

where ϖ is a logical switch between two-dimensional ($\varpi = 0$) and axisymmetric ($\varpi = 1$) equations and,

$$\varpi_a = 1 - \varpi + \varpi y \quad (2)$$

is 1 for two dimensions and y for axisymmetric.

The conserved state vector is,

$$\mathbf{U} = (\rho,\ \rho u,\ \rho v,\ \rho E)^\intercal \quad (3)$$

The inviscid and viscous fluxes are,

$$\vec{\mathbf{F}}^i = \begin{pmatrix} \rho\vec{V} \\ \rho u\vec{V} + (1,0)P \\ \rho v\vec{V} + (0,1)P \\ \rho\vec{V}H \end{pmatrix} \quad (4)$$

$$\vec{\mathbf{F}}^v = \frac{1}{R_{e_\infty}} \begin{pmatrix} 0 \\ \boldsymbol{\tau} \\ \kappa\vec{\nabla}T + \vec{V}\boldsymbol{\tau} \end{pmatrix} \quad (5)$$

with the shear-stress tensor defined,

$$\boldsymbol{\tau} = \mu\left[\vec{\nabla}^\intercal\vec{V} + \left(\vec{\nabla}^\intercal\vec{V}\right)^\intercal - \frac{2}{3}\vec{\nabla}\cdot\vec{V}I\right] \quad (6)$$

The inviscid and viscous axisymmetric source terms each have only one non-zero term,

$$B_3^i = P, \qquad B_3^v = \frac{2\mu}{3R_{e_\infty}}\left(2\frac{v}{y} - \vec{\nabla}\cdot\vec{V}\right) \quad (7)$$

The governing equations are discretized using two different, second-order node-based schemes for unstructured (triangulated) meshes. The popular Barth[5,6] finite volume scheme is chosen as the baseline for comparison. The other scheme is the multi-dimensional-upwind fluctuation splitting discretization due to Sidilkover,[7–9] extended here to include eigen-value limiting, axisymmetric terms, and both thin-layer and full Navier-Stokes viscous terms.

State Vector

In the finite volume context, integration of the dependent variables over the control volume about node i is performed as,

$$\int_{\Omega_i} \varpi_a \mathbf{U}_t\, d\Omega = \overline{\varpi}_a S_i \mathbf{U}_{i_t} \quad (8)$$

For two-dimensional $\overline{\varpi}_a = 1$, while for axisymmetric $\overline{\varpi}_a$ can be either taken as $\overline{\varpi}_a = y_i$, for mass-lumping to the node, or as the y-value of the centroid of Ω_i.

In the fluctuation splitting context, the parameter vector is taken to vary linearly over each element. For a perfect gas, changes to the conserved variables can be related to changes in the parameter vector as,

$$d\mathbf{U} = \mathbf{U}_Z\, d\mathbf{Z} \quad (9)$$

$$\mathbf{U}_Z = \begin{bmatrix} 2Z_1 & 0 & 0 & 0 \\ Z_2 & Z_1 & 0 & 0 \\ Z_3 & 0 & Z_1 & 0 \\ \frac{1}{\gamma}Z_4 & \frac{\gamma-1}{\gamma}Z_2 & \frac{\gamma-1}{\gamma}Z_3 & \frac{1}{\gamma}Z_1 \end{bmatrix} \quad (10)$$

Integration of $\varpi_a \mathbf{U}_t$ over an element leads to a mass matrix,

$$\int_\Omega \varpi_a \mathbf{U}_t\, d\Omega = \int_\Omega \varpi_a \mathbf{U}_Z \mathbf{Z}_t\, d\Omega \quad (11)$$

If mass-lumping to the nodes is employed, introducing temporal, but not spatial, errors, Eqn. 11 can be partitioned among the three nodes defining Ω as,

$$\int_\Omega \varpi_a \mathbf{U}_t \, d\Omega \; = \frac{S_\mathsf{T}}{3} \sum_{i=1}^{3} \varpi_{a_i} \mathbf{U}_{i_t} \tag{12}$$

so that the sum of all contributions to node i equals $\varpi_{a_i} S_i \mathbf{U}_{i_t}$.

Axisymmetric Sources

In the finite volume framework, the inviscid axisymmetric source term, $\mathbf{B}^i$, is simply evaluated at the node as,

$$\int_{\Omega_j} \mathbf{B}^i \, d\Omega \; = S_j \mathbf{B}^i_j \tag{13}$$

While some authors insist on upwinding source terms for fluctuation splitting,[8,10] the present analysis considers an upwind distribution to be inappropriate for the axisymmetric source terms, which arise from purely geometric manipulations. The axisymmetric source term can be distributed to the node in the fluctuation splitting framework following a mass-lumped analogy as,

$$\varpi_{a_j} S_j \mathbf{U}_{j_t} \; \leftarrow \varpi S_j \mathbf{B}^i_j \tag{14}$$

which is equivalent to the finite volume treatment of Eqn. 13. A modification of this distribution is to send contributions weighted by the averaged values,

$$\varpi_{a_j} S_j \mathbf{U}_{j_t} \; \leftarrow \varpi \frac{S_\mathsf{T}}{3} \tilde{\mathbf{B}}^i_\mathsf{T} + COE \tag{15}$$

A more rigorous treatment integrates the source term analytically, based on a linear variation of the parameter vector. The only non-zero inviscid source term is,

$$B^i_3 \; = P = \frac{\gamma - 1}{\gamma} \left(Z_1 Z_4 - \frac{Z_2^2 + Z_3^2}{2} \right) \tag{16}$$

The integration over the triangular element is divided into thirds along the median-dual boundaries, as in Figure 1, so that,

$$\Omega \; = \Omega_1 + \Omega_2 + \Omega_3 \tag{17}$$

The subintegrals are then distributed to the nearest node. Notice that the subdivided integration elements, Ω_{1-3}, are quadrilaterals, whereas the original element was a triangle. The distribution formula is thus,

$$\varpi_{a_j} S_j \mathbf{U}_{j_t} \; \leftarrow \varpi \int_{\Omega_j} \mathbf{B}^i \, d\Omega_j + COE \tag{18}$$

The integration of the source term over Ω_j is expanded in detail in Ref. 11.

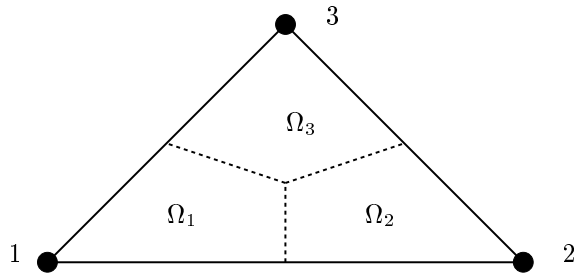

Fig. 1 Subdivision of triangular element into three quadrilateral integration areas. Dashed lines are the median-dual mesh.

The viscous axisymmetric source can be integrated using the Haselbacher[12] thin-layer approach (detailed in the following viscous flux section) as,

$$\int_{\Omega_i} B^v_3 \, d\Omega \; = \frac{4}{3R_{e_\infty}} \int_{\Omega_i} \frac{\mu v}{y} \, d\Omega - \frac{2}{3R_{e_\infty}} \oint_{\Gamma_i} \mu \vec{V} \cdot \hat{n} \, d\Gamma \tag{19}$$

Mass lumping to the node for the first term yields,

$$\int_{\Omega_i} \frac{\mu v}{y} \, d\Omega \; = \mu_i S_i \frac{v_i}{y_i} \tag{20}$$

while the second term is evaluated at edge midpoints.

Inviscid Flux

The finite volume discretization of the inviscid flux is performed as an average of the fluxes to the left and right of the control volume face, times the parameter ϖ_a (equal to 1 for two-dimensional or the y-value of the quadrature point on the face for axisymmetric) plus the artificial dissipation, which is defined as,

$$\mathbf{\Phi} \; = \frac{1}{2} |\tilde{\vec{\mathbf{A}}} \cdot \hat{\mathbf{n}}| (\mathbf{U}_\mathsf{R} - \mathbf{U}_\mathsf{L}) \tag{21}$$

where by convention the right state is to the outside of the control volume while the left state is to the inside.

The parameter vector, $\mathbf{Z} = \sqrt{\rho} \, [1, u, v, H]^T$, is linearly averaged, $\bar{\mathbf{Z}} = \frac{1}{2}(\mathbf{Z}_\mathsf{L} + \mathbf{Z}_\mathsf{R})$, to provide the quantities,

$$\tilde{u} \; = \frac{\bar{Z}_2}{\bar{Z}_1}, \qquad \tilde{v} = \frac{\bar{Z}_3}{\bar{Z}_1}, \qquad \tilde{H} = \frac{\bar{Z}_4}{\bar{Z}_1} \tag{22}$$

and the Roe-density is, $\tilde{\rho} = \sqrt{\rho_\mathsf{L} \rho_\mathsf{R}}$.

The projected flux Jacobian is decomposed as,

$$|\tilde{\vec{\mathbf{A}}} \cdot \hat{\mathbf{n}}| \; = \tilde{\mathbf{X}} |\tilde{\mathbf{\Lambda}}| \tilde{\mathbf{X}}^{-1} \tag{23}$$

with,

$$\mathbf{\Lambda} \; = \mathrm{diag}\,(\mathcal{V}, \, \mathcal{V}, \, \mathcal{V} + a, \, \mathcal{V} - a) \tag{24}$$

$$\mathbf{X} \; = \begin{bmatrix} 1 & 0 & 1 & 1 \\ u & -n^\mathsf{y} & u + an^\mathsf{x} & u - an^\mathsf{x} \\ v & n^\mathsf{x} & v + an^\mathsf{y} & v - an^\mathsf{y} \\ \frac{V^2}{2} & vn^\mathsf{x} - un^\mathsf{y} & H + a\mathcal{V} & H - a\mathcal{V} \end{bmatrix} \tag{25}$$

The product $\tilde{\mathbf{X}}^{-1}(\mathbf{U}_\mathsf{R} - \mathbf{U}_\mathsf{L})$ is expressed,

$$\tilde{\mathbf{X}}^{-1} d\mathbf{U} = \frac{1}{2\tilde{a}^2} \begin{pmatrix} 2\tilde{a}^2 d\rho - 2dP \\ 2\tilde{a}^2 (n^x dv - n^y du) \\ dP + \tilde{\rho}\tilde{a}\, d\mathcal{V} \\ dP - \tilde{\rho}\tilde{a}\, d\mathcal{V} \end{pmatrix} \tag{26}$$

where the projected velocity is $\mathcal{V} = \vec{V} \cdot \hat{n}$ and the averaged speed of sound for a perfect gas is,

$$\tilde{a}^2 = (\gamma - 1)\left(\tilde{H} - \frac{\tilde{u}^2 + \tilde{v}^2}{2}\right) \tag{27}$$

Integration of the inviscid flux for fluctuation splitting is performed as,

$$\int_\Omega \vec{\nabla} \cdot \left(\varpi_a \vec{\mathbf{F}}^i\right) d\Omega = \int_\Omega \varpi_a \vec{\nabla} \cdot \vec{\mathbf{F}}^i \, d\Omega + \varpi \int_\Omega \mathbf{F}^{i^y} \, d\Omega \tag{28}$$

The y-component of the flux function can be written in terms of the parameter vector as,

$$\mathbf{F}^{i^y} = \begin{bmatrix} Z_1 Z_3 \\ Z_2 Z_3 \\ Z_3^2 + \frac{\gamma-1}{\gamma}\left(Z_1 Z_4 - \frac{Z_2^2 + Z_3^2}{2}\right) \\ Z_3 Z_4 \end{bmatrix} \tag{29}$$

A linear variation of the parameter vector over a triangular element can be represented as,

$$\begin{aligned} \mathbf{Z}(x,y) = &\frac{1}{2S_\mathsf{T}} \epsilon_{ijk} \mathbf{Z}_j \\ &\cdot [(x - x_i)(y_k - y_i) + (y - y_i)(x_i - x_k)] \end{aligned} \tag{30}$$

where ϵ_{ijk} is the cyclic-permutation summation operator. The linear variation can also be written in the element-local (ξ, η) coordinates, referring to Figure 2, as,

$$\begin{aligned} \mathbf{Z}(\xi,\eta) &= \mathbf{Z}_1 + \frac{1}{\ell_3}(\mathbf{Z}_2 - \mathbf{Z}_1)\xi + \frac{1}{\ell_1}(\mathbf{Z}_3 - \mathbf{Z}_2)\eta \\ &= \mathbf{Z}_1 + \frac{1}{\ell_3}\Delta_\xi \mathbf{Z}\, \xi + \frac{1}{\ell_1}\Delta_\eta \mathbf{Z}\, \eta \end{aligned} \tag{31}$$

The domain is on $0 \le \eta \le \frac{\ell_1}{\ell_3}\xi$ and $0 \le \xi \le \ell_3$. The cartesian coordinates map similarly,

$$x(\xi,\eta) = x_1 + \frac{1}{\ell_3}\Delta_\xi x\, \xi + \frac{1}{\ell_1}\Delta_\eta x\, \eta \tag{32}$$

$$y(\xi,\eta) = y_1 + \frac{1}{\ell_3}\Delta_\xi y\, \xi + \frac{1}{\ell_1}\Delta_\eta y\, \eta \tag{33}$$

Some general integration rules can be developed for linear variations over the triangular elements:

$$\int_\Omega d\Omega = S_\mathsf{T} \tag{34}$$

$$\int_\Omega x \, d\Omega = S_\mathsf{T} \bar{x} \tag{35}$$

$$\int_\Omega xy \, d\Omega = S_\mathsf{T} \bar{x}\bar{y} - \frac{S_\mathsf{T}}{4}\left(\bar{x}\bar{y} - \frac{1}{3}\sum_{j=1}^{3} x_j y_j\right) \tag{36}$$

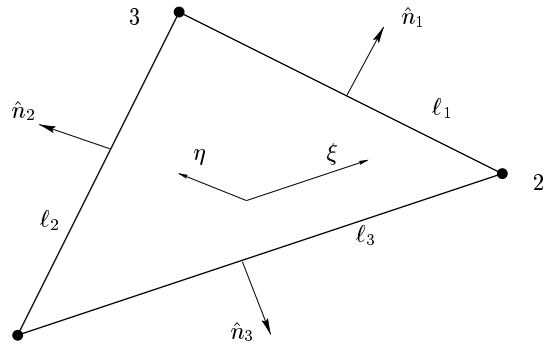

Fig. 2 Elemental triangular domain for fluctuation splitting.

The cell-averaged value is,

$$\bar{x} = \frac{x_1 + x_2 + x_3}{3} = \frac{1}{3}\sum_{j=1}^{3} x_j \tag{37}$$

The last term of Eqn. 28 is distributed to the nodes in a manner similar to the source term,

$$\varpi_{a_i} S_i \mathbf{U}_{i_t} \leftarrow -\varpi \int_{\Omega_i} \mathbf{F}^{i^y} \, d\Omega_i + COE \tag{38}$$

This integral can be evaluated exactly as,

$$\begin{aligned} \int_{\Omega_i} Z_1 Z_3 \, d\Omega_i = \frac{S_\mathsf{T}}{144} \Bigg[&14 \bar{Z}_1 \bar{Z}_3 + 11(Z_{1_i} \bar{Z}_3 + \bar{Z}_1 Z_{3_i}) \\ &+ 9 Z_{1_i} Z_{3_i} + \sum_{j=1}^{3} Z_{1_j} Z_{3_j} \Bigg] \end{aligned} \tag{39}$$

for the continuity equation. The integrals for the other governing equations follow directly from Eqn. 39.

The remaining term to evaluate in Eqn. 28 is the inviscid fluctuation,

$$\begin{aligned} \phi &= -\int_\Omega \varpi_a \vec{\nabla} \cdot \vec{\mathbf{F}}^i \, d\Omega \\ &= -\frac{\ell_1 \ell_3}{2S_\mathsf{T}} \int_\Omega \varpi_a \left(\hat{n}_1 \cdot \vec{\mathbf{F}}^i_\xi - \hat{n}_3 \cdot \vec{\mathbf{F}}^i_\eta\right) d\Omega \\ &= -\frac{1}{2S_\mathsf{T}} \int_\Omega \varpi_a \left(\ell_1 \hat{n}_1 \cdot \vec{\mathbf{F}}_Z \Delta_\xi \mathbf{Z} - \ell_3 \hat{n}_3 \cdot \vec{\mathbf{F}}_Z \Delta_\eta \mathbf{Z}\right) d\Omega \end{aligned} \tag{40}$$

where $d\vec{\mathbf{F}}^i = \vec{\mathbf{F}}_Z \, d\mathbf{Z}$ and,

$$\vec{\mathbf{F}}^{\mathsf{x}}_Z = \begin{bmatrix} Z_2 & Z_1 & 0 & 0 \\ \frac{\gamma-1}{\gamma} Z_4 & \frac{\gamma+1}{\gamma} Z_2 & -\frac{\gamma-1}{\gamma} Z_3 & \frac{\gamma-1}{\gamma} Z_1 \\ 0 & Z_3 & Z_2 & 0 \\ 0 & Z_4 & 0 & Z_2 \end{bmatrix} \tag{41}$$

$$\vec{\mathbf{F}}^{\mathsf{y}}_Z = \begin{bmatrix} Z_3 & 0 & Z_1 & 0 \\ 0 & Z_3 & Z_2 & 0 \\ \frac{\gamma-1}{\gamma} Z_4 & -\frac{\gamma-1}{\gamma} Z_2 & \frac{\gamma+1}{\gamma} Z_3 & \frac{\gamma-1}{\gamma} Z_1 \\ 0 & 0 & Z_4 & Z_3 \end{bmatrix} \tag{42}$$

The integration rule Eqn. 36 allows for the direct evaluation of Eqn. 40 as,

$$\begin{aligned}\boldsymbol{\phi} = &-\frac{1}{2}\overline{\varpi}_a \ell_1 \hat{n}_1 \cdot \left[\overline{\vec{\mathbf{F}}}_Z - \frac{1}{4}\left(\overline{\vec{\mathbf{F}}}_Z - \frac{1}{3}\sum_{j=1}^{3}\frac{\varpi_{a_j}}{\overline{\varpi}_a}\vec{\mathbf{F}}_{Z_j}\right)\right]\Delta_\xi \mathbf{Z} \\ &+ \frac{1}{2}\overline{\varpi}_a \ell_3 \hat{n}_3 \\ &\cdot \left[\overline{\vec{\mathbf{F}}}_Z - \frac{1}{4}\left(\overline{\vec{\mathbf{F}}}_Z - \frac{1}{3}\sum_{j=1}^{3}\frac{\varpi_{a_j}}{\overline{\varpi}_a}\vec{\mathbf{F}}_{Z_j}\right)\right]\Delta_\eta \mathbf{Z}\end{aligned} \tag{43}$$

Noting that $\tilde{\vec{\mathbf{A}}} = \overline{\vec{\mathbf{F}}}_{\mathbf{Z}}\,\mathbf{Z}_{\tilde{\mathbf{U}}}$ and,

$$\mathbf{Z}_U = \frac{1}{2\sqrt{\rho}}\begin{bmatrix} 1 & 0 & 0 & 0 \\ -u & 2 & 0 & 0 \\ -v & 0 & 2 & 0 \\ -H+(\gamma-1)(u^2+v^2) & -2(\gamma-1)u & -2(\gamma-1)v & 2\gamma \end{bmatrix} \tag{44}$$

with the tilde-averaged quantities defined as,

$$\tilde{\mathbf{U}} = \mathbf{U}(\bar{\mathbf{Z}}),\ \widetilde{\Delta_\xi \mathbf{U}} = \mathbf{U}_{\bar{Z}}\,\Delta_\xi \mathbf{Z},\ \widetilde{\Delta_\eta \mathbf{U}} = \mathbf{U}_{\bar{Z}}\,\Delta_\eta \mathbf{Z} \tag{45}$$

leads to the fluctuation expressed as,

$$\begin{aligned}\boldsymbol{\phi} = &-\frac{1}{2}\overline{\varpi}_a \ell_1 \hat{n}_1 \cdot \left[\tilde{\vec{\mathbf{A}}} - \frac{\mathbf{1}}{\mathbf{4}}\left(\tilde{\vec{\mathbf{A}}} - \frac{\mathbf{1}}{\mathbf{3}}\sum_{\mathbf{j=1}}^{\mathbf{3}}\frac{\varpi_{\mathbf{a_j}}}{\overline{\varpi}_{\mathbf{a}}}\tilde{\mathbf{A}}_{\mathbf{j}}\right)\right]\widetilde{\Delta_\xi \mathbf{U}} \\ &+ \frac{1}{2}\overline{\varpi}_a \ell_3 \hat{n}_3 \cdot \left[\tilde{\vec{\mathbf{A}}} - \frac{\mathbf{1}}{\mathbf{4}}\left(\tilde{\vec{\mathbf{A}}} - \frac{\mathbf{1}}{\mathbf{3}}\sum_{\mathbf{j=1}}^{\mathbf{3}}\frac{\varpi_{\mathbf{a_j}}}{\overline{\varpi}_{\mathbf{a}}}\tilde{\mathbf{A}}_{\mathbf{j}}\right)\right]\widetilde{\Delta_\eta \mathbf{U}} \\ = &\,\boldsymbol{\phi}^\xi + \boldsymbol{\phi}^\eta\end{aligned} \tag{46}$$

Equation 46 includes the approximation,

$$\vec{\mathbf{A}}_j \simeq \vec{\mathbf{F}}_{Z_j}\mathbf{Z}_{\tilde{U}} \tag{47}$$

A transformation of variables can be made to the auxiliary variables so that,

$$\boldsymbol{\phi} = \tilde{\mathbf{U}}_W \breve{\boldsymbol{\phi}} \tag{48}$$

with,

$$\mathbf{U}_W = \begin{bmatrix} 1 & 0 & 0 & \frac{1}{a^2} \\ u & 1 & 0 & \frac{1}{a^2}u \\ v & 0 & 1 & \frac{1}{a^2}v \\ \frac{V^2}{2} & u & v & \frac{1}{\gamma-1}\frac{T_0}{T} \end{bmatrix} \tag{49}$$

Similarity transformations lead to,

$$\begin{aligned}\breve{\boldsymbol{\phi}} = &-\frac{1}{2}\overline{\varpi}_a \ell_1 \hat{n}_1 \cdot \left[\tilde{\vec{\boldsymbol{\mathcal{A}}}} - \frac{1}{4}\left(\tilde{\vec{\boldsymbol{\mathcal{A}}}} - \frac{1}{3}\sum_{j=1}^{3}\frac{\varpi_{a_j}}{\overline{\varpi}_a}\vec{\boldsymbol{\mathcal{A}}}_j\right)\right]\widetilde{\Delta_\xi \mathbf{W}} \\ &+ \frac{1}{2}\overline{\varpi}_a \ell_3 \hat{n}_3 \cdot \left[\tilde{\vec{\boldsymbol{\mathcal{A}}}} - \frac{1}{4}\left(\tilde{\vec{\boldsymbol{\mathcal{A}}}} - \frac{1}{3}\sum_{j=1}^{3}\frac{\varpi_{a_j}}{\overline{\varpi}_a}\vec{\boldsymbol{\mathcal{A}}}_j\right)\right]\widetilde{\Delta_\eta \mathbf{W}} \\ = &-\overline{\varpi}_a\left(\boldsymbol{\alpha}\,\widetilde{\Delta_\xi \mathbf{W}} + \boldsymbol{\beta}\,\widetilde{\Delta_\eta \mathbf{W}}\right) \\ = &\,\breve{\boldsymbol{\phi}}^\xi + \breve{\boldsymbol{\phi}}^\eta\end{aligned} \tag{50}$$

with $\vec{\boldsymbol{\mathcal{A}}} = \mathbf{W}_U \vec{\mathbf{A}} \mathbf{U}_W$ and,

$$\widetilde{\Delta_\xi \mathbf{W}} = \mathbf{W}_{\tilde{U}}\,\widetilde{\Delta_\xi \mathbf{U}} = \mathbf{W}_{\bar{Z}}\,\Delta_\xi \mathbf{Z} \tag{51}$$

$$\widetilde{\Delta_\eta \mathbf{W}} = \mathbf{W}_{\tilde{U}}\,\widetilde{\Delta_\eta \mathbf{U}} = \mathbf{W}_{\bar{Z}}\,\Delta_\eta \mathbf{Z} \tag{52}$$

where,

$$\mathbf{W}_U = \begin{bmatrix} 2 - \frac{T_0}{T} & \frac{u}{h} & \frac{v}{h} & -\frac{1}{h} \\ -u & 1 & 0 & 0 \\ -v & 0 & 1 & 0 \\ \frac{\gamma-1}{2}V^2 & -(\gamma-1)u & -(\gamma-1)v & \gamma-1 \end{bmatrix} \tag{53}$$

$$\begin{aligned}\mathbf{W}_Z &= \sqrt{\rho}\begin{bmatrix} 2 - \frac{H}{\gamma h} & \frac{u}{\gamma h} & \frac{v}{\gamma h} & -\frac{1}{\gamma h} \\ -u & 1 & 0 & 0 \\ -v & 0 & 1 & 0 \\ \frac{\gamma-1}{\gamma}H & -\frac{\gamma-1}{\gamma}u & -\frac{\gamma-1}{\gamma}v & \frac{\gamma-1}{\gamma} \end{bmatrix} \\ &= \begin{bmatrix} 2Z_1 - \frac{\gamma-1}{\gamma a^2}Z_4 & \frac{\gamma-1}{\gamma a^2}Z_2 & \frac{\gamma-1}{\gamma a^2}Z_3 & -\frac{\gamma-1}{\gamma a^2}Z_1 \\ -Z_2 & Z_1 & 0 & 0 \\ -Z_3 & 0 & Z_1 & 0 \\ \frac{\gamma-1}{\gamma}Z_4 & -\frac{\gamma-1}{\gamma}Z_2 & -\frac{\gamma-1}{\gamma}Z_3 & \frac{\gamma-1}{\gamma}Z_1 \end{bmatrix}\end{aligned} \tag{54}$$

using the relation,

$$h = c_p T = \frac{a^2}{\gamma - 1} \tag{55}$$

The projection of $\vec{\boldsymbol{\mathcal{A}}}$ has the simple form,

$$\hat{n}\cdot\vec{\boldsymbol{\mathcal{A}}} = \begin{bmatrix} \mathcal{V} & 0 & 0 & 0 \\ 0 & \mathcal{V} & 0 & n^{\mathsf{x}} \\ 0 & 0 & \mathcal{V} & n^{\mathsf{y}} \\ 0 & a^2 n^{\mathsf{x}} & a^2 n^{\mathsf{y}} & \mathcal{V} \end{bmatrix} \tag{56}$$

where the projected velocity is $\mathcal{V} = \hat{n}\cdot\vec{V}$. The generalized advection speeds are,

$$\boldsymbol{\alpha} = \frac{\ell_1}{2}\hat{n}_1 \cdot \left[\tilde{\vec{\boldsymbol{\mathcal{A}}}} - \frac{1}{4}\left(\tilde{\vec{\boldsymbol{\mathcal{A}}}} - \frac{1}{3}\sum_{j=1}^{3}\frac{\varpi_{a_j}}{\overline{\varpi}_a}\vec{\boldsymbol{\mathcal{A}}}_j\right)\right] \tag{57}$$

$$\boldsymbol{\beta} = -\frac{\ell_3}{2}\hat{n}_3 \cdot \left[\tilde{\vec{\boldsymbol{\mathcal{A}}}} - \frac{1}{4}\left(\tilde{\vec{\boldsymbol{\mathcal{A}}}} - \frac{1}{3}\sum_{j=1}^{3}\frac{\varpi_{a_j}}{\overline{\varpi}_a}\vec{\boldsymbol{\mathcal{A}}}_j\right)\right] \tag{58}$$

where the approximation $\vec{\mathcal{A}}_j = \mathbf{W}_{\tilde{U}} \vec{\mathbf{A}}_j \tilde{\mathbf{U}}_W$ has been incorporated.

Linearity preservation for second-order spatial accuracy is obtained by limiting the fluctuations componentwise,

$$\breve{\phi}_j^{*^\xi} = \breve{\phi}_j^\xi + \breve{\phi}_j^\eta \, \psi(Q_j) = \breve{\phi}_j^\xi \left(1 - \psi\left(\frac{1}{Q_j}\right)\right) \quad (59)$$

$$\breve{\phi}_j^{*^\eta} = \breve{\phi}_j^\eta - \breve{\phi}_j^\eta \, \psi(Q_j) = \breve{\phi}_j^\eta \, (1 - \psi\,(Q_j)) \quad (60)$$

where the second equalities hold for symmetric limiters. The limiting ratio is,

$$Q_j = -\frac{\breve{\phi}_j^\xi}{\breve{\phi}_j^\eta} \quad (61)$$

In vector form, Eqns. 59 and 60 can be written,

$$\breve{\boldsymbol{\phi}}^{*^\xi} = \mathbf{D}^\xi \breve{\boldsymbol{\phi}}^\xi \quad (62)$$

$$\breve{\boldsymbol{\phi}}^{*^\eta} = \mathbf{D}^\eta \breve{\boldsymbol{\phi}}^\eta \quad (63)$$

with

$$\mathbf{D}^\xi = \mathrm{diag}\left(1 - \psi\left(\frac{1}{Q_j}\right)\right) \quad (64)$$

$$\mathbf{D}^\eta = \mathrm{diag}\,(1 - \psi\,(Q_j)) \quad (65)$$

Upwinding is achieved through the introduction of artificial dissipation

$$\breve{\boldsymbol{\phi}}'^\xi = \mathrm{sign}(\boldsymbol{\alpha}) \breve{\boldsymbol{\phi}}^{*^\xi} = -\overline{\overline{\omega}}_a \mathbf{M}_\alpha \mathbf{D}^\xi \mathbf{M}_\alpha^{-1} |\boldsymbol{\alpha}| \, \widetilde{\Delta_\xi \mathbf{W}} \quad (66)$$

$$\breve{\boldsymbol{\phi}}'^\eta = \mathrm{sign}(\boldsymbol{\beta}) \breve{\boldsymbol{\phi}}^{*^\eta} = -\overline{\overline{\omega}}_a \mathbf{M}_\beta \mathbf{D}^\eta \mathbf{M}_\beta^{-1} |\boldsymbol{\beta}| \, \widetilde{\Delta_\eta \mathbf{W}} \quad (67)$$

where $\mathbf{M}_\alpha = \mathrm{sign}(\boldsymbol{\alpha})$ and $\mathbf{M}_\beta = \mathrm{sign}(\boldsymbol{\beta})$. The absolute values of the generalized advection speeds are developed using the following decomposition, which is exact for the two-dimensional equations but approximate for the axisymmetric form,

$$\boldsymbol{\alpha} = \frac{\ell_1}{2} \hat{n}_1 \cdot \tilde{\boldsymbol{\mathcal{A}}} = \frac{\ell_1}{2} \tilde{\boldsymbol{\mathcal{X}}} \tilde{\boldsymbol{\Lambda}} \tilde{\boldsymbol{\mathcal{X}}}^{-1} \quad (68)$$

where $\boldsymbol{\Lambda}$ remains as in Eqn. 24 and,

$$\boldsymbol{\mathcal{X}} = \begin{bmatrix} 1 & 0 & 0 & 0 \\ 0 & \hat{n}^{\mathsf{y}} & \hat{n}^{\mathsf{x}} & \hat{n}^{\mathsf{x}} \\ 0 & -\hat{n}^{\mathsf{x}} & \hat{n}^{\mathsf{y}} & \hat{n}^{\mathsf{y}} \\ 0 & 0 & a & -a \end{bmatrix} \quad (69)$$

The absolute value is then defined as,

$$|\boldsymbol{\alpha}| = \frac{\ell_1}{2} \tilde{\boldsymbol{\mathcal{X}}} |\tilde{\boldsymbol{\Lambda}}| \tilde{\boldsymbol{\mathcal{X}}}^{-1} \quad (70)$$

Expressions for the sign of the generalized wavespeeds are developed from,

$$|\boldsymbol{\alpha}| = \mathbf{M}_\alpha \boldsymbol{\alpha} \quad (71)$$

$$\mathbf{M}_\alpha = \tilde{\boldsymbol{\mathcal{X}}} |\tilde{\boldsymbol{\Lambda}}| \tilde{\boldsymbol{\Lambda}}^{-1} \tilde{\boldsymbol{\mathcal{X}}}^{-1} \quad (72)$$

which for $|\tilde{\mathcal{V}}_\alpha| > \tilde{a}$ leads to,

$$\mathbf{M}_\alpha = \mathrm{sign}(\tilde{\mathcal{V}}_\alpha) I \quad (73)$$

and for $|\tilde{\mathcal{V}}_\alpha| < \tilde{a}$,

$$\mathbf{M}_\alpha = \begin{bmatrix} \mathrm{sign}(\tilde{\mathcal{V}}_\alpha) & 0 & 0 & 0 \\ 0 & n_1^{\mathsf{y}^2} \mathrm{sign}(\tilde{\mathcal{V}}_\alpha) & -n_1^{\mathsf{x}} n_1^{\mathsf{y}} \mathrm{sign}(\tilde{\mathcal{V}}_\alpha) & \frac{n_1^{\mathsf{x}}}{\tilde{a}} \\ 0 & -n_1^{\mathsf{x}} n_1^{\mathsf{y}} \mathrm{sign}(\tilde{\mathcal{V}}_\alpha) & n_1^{\mathsf{x}^2} \mathrm{sign}(\tilde{\mathcal{V}}_\alpha) & \frac{n_1^{\mathsf{y}}}{\tilde{a}} \\ 0 & \tilde{a} n_1^{\mathsf{x}} & \tilde{a} n_1^{\mathsf{y}} & 0 \end{bmatrix} \quad (74)$$

where $\mathcal{V}_\alpha = \hat{n}_1 \cdot \vec{V}$. Similarly, defining $|\boldsymbol{\beta}|$ as,

$$|\boldsymbol{\beta}| = -\frac{\ell_3}{2} \tilde{\boldsymbol{\mathcal{X}}} |\tilde{\boldsymbol{\Lambda}}| \tilde{\boldsymbol{\mathcal{X}}}^{-1} \quad (75)$$

for $|\tilde{\mathcal{V}}_\beta| > \tilde{a}$ leads to,

$$\mathbf{M}_\beta = \mathrm{sign}(\tilde{\mathcal{V}}_\beta) I \quad (76)$$

and for $|\tilde{\mathcal{V}}_\beta| < \tilde{a}$,

$$\mathbf{M}_\beta = \begin{bmatrix} \mathrm{sign}(\tilde{\mathcal{V}}_\beta) & 0 & 0 & 0 \\ 0 & n_3^{\mathsf{y}^2} \mathrm{sign}(\tilde{\mathcal{V}}_\beta) & -n_3^{\mathsf{x}} n_3^{\mathsf{y}} \mathrm{sign}(\tilde{\mathcal{V}}_\beta) & \frac{n_3^{\mathsf{x}}}{\tilde{a}} \\ 0 & -n_3^{\mathsf{x}} n_3^{\mathsf{y}} \mathrm{sign}(\tilde{\mathcal{V}}_\beta) & n_3^{\mathsf{x}^2} \mathrm{sign}(\tilde{\mathcal{V}}_\beta) & \frac{n_3^{\mathsf{y}}}{\tilde{a}} \\ 0 & \tilde{a} n_3^{\mathsf{x}} & \tilde{a} n_3^{\mathsf{y}} & 0 \end{bmatrix} \quad (77)$$

where $\mathcal{V}_\beta = \hat{n}_3 \cdot \vec{V}$. $\mathbf{M}_\alpha$ and $\mathbf{M}_\beta$ have the property,

$$\mathbf{M}_\alpha^{-1} = \mathbf{M}_\alpha \qquad \mathbf{M}_\beta^{-1} = \mathbf{M}_\beta \quad (78)$$

Eigen-value limiting for the suppression of expansion shocks can be introduced into Eqn. 70. If the limited eigen-value is expressed as,

$$|\Lambda|_{lim} = |\Lambda| + \delta_\Lambda \quad (79)$$

then the additional artificial dissipation for eigen-value limiting in the ξ direction to be added to Eqn. 66 is, with $\delta^+ = \frac{1}{2}(\delta_{\Lambda_3} + \delta_{\Lambda_4})$ and $\delta^- = \frac{1}{2}(\delta_{\Lambda_3} - \delta_{\Lambda_4})$,

$$-\bar{\overline{\omega}}_a \frac{\ell_1}{2} \cdot \begin{bmatrix} \delta_{\Lambda_1} & 0 & 0 & 0 \\ 0 & n_1^{\mathsf{x}^2} \delta^+ + n_1^{\mathsf{y}^2} \delta_{\Lambda_2} & n_1^{\mathsf{x}} n_1^{\mathsf{y}} (\delta^+ - \delta_{\Lambda_2}) & \frac{n_1^{\mathsf{x}}}{a} \delta^- \\ 0 & n_1^{\mathsf{x}} n_1^{\mathsf{y}} (\delta^+ - \delta_{\Lambda_2}) & n_1^{\mathsf{x}^2} \delta_{\Lambda_2} + n_1^{\mathsf{y}^2} \delta^+ & \frac{n_1^{\mathsf{y}}}{a} \delta^- \\ 0 & a n_1^{\mathsf{x}} \delta^- & a n_1^{\mathsf{y}} \delta^- & \delta^+ \end{bmatrix} \cdot \widetilde{\Delta_\xi W} \quad (80)$$

while the eigen-value limiting in the η direction takes

the form,

$$+ \bar{\varpi}_a \frac{\ell_3}{2} \cdot \begin{bmatrix} \delta_{\Lambda_1} & 0 & 0 & 0 \\ 0 & n_3^{x^2}\delta^+ + n_3^{y^2}\delta_{\Lambda_2} & n_3^x n_3^y(\delta^+ - \delta_{\Lambda_2}) & \frac{n_3^x}{a}\delta^- \\ 0 & n_3^x n_3^y(\delta^+ - \delta_{\Lambda_2}) & n_3^{x^2}\delta_{\Lambda_2} + n_3^{y^2}\delta^+ & \frac{n_3^y}{a}\delta^- \\ 0 & a n_3^x \delta^- & a n_3^y \delta^- & \delta^+ \end{bmatrix} \cdot \widetilde{\Delta_\eta W} \quad (81)$$

The fluctuation is distributed to the nodes using,

$$\begin{aligned} S_1\mathbf{U}_{1_t} &\leftarrow \frac{1}{2}(\boldsymbol{\phi}^{*^\xi} - \boldsymbol{\phi}'^{^\xi}) + COE \\ S_2\mathbf{U}_{2_t} &\leftarrow \frac{1}{2}(\boldsymbol{\phi}^{*^\xi} + \boldsymbol{\phi}'^{^\xi}) + \frac{1}{2}(\boldsymbol{\phi}^{*^\eta} + \boldsymbol{\phi}'^{^\eta}) + COE \\ S_3\mathbf{U}_{3_t} &\leftarrow \frac{1}{2}(\boldsymbol{\phi}^{*^\eta} - \boldsymbol{\phi}'^{^\eta}) + COE \end{aligned} \quad (82)$$

where COE stands for contributions from other elements. The distribution can be expressed in a more compact form,

$$\begin{aligned} S_i\mathbf{U}_{i_t} \leftarrow \frac{1}{4}\Big[& i(3-i)(\boldsymbol{\phi}^{*^\xi} + (-1)^i \boldsymbol{\phi}'^{^\xi}) \\ & + (-4+5i-i^2)(\boldsymbol{\phi}^{*^\eta} + (-1)^i \boldsymbol{\phi}'^{^\eta})\Big] \\ & + COE \qquad\qquad i = 1,2,3 \end{aligned} \quad (83)$$

where Eqn. 48 is used to define,

$$\boldsymbol{\phi}^{*^\xi} = \tilde{\mathbf{U}}_W \breve{\boldsymbol{\phi}}^{*^\xi}, \qquad \boldsymbol{\phi}'^{^\xi} = \tilde{\mathbf{U}}_W \breve{\boldsymbol{\phi}}'^{^\xi} \quad (84)$$

$$\boldsymbol{\phi}^{*^\eta} = \tilde{\mathbf{U}}_W \breve{\boldsymbol{\phi}}^{*^\eta}, \qquad \boldsymbol{\phi}'^{^\eta} = \tilde{\mathbf{U}}_W \breve{\boldsymbol{\phi}}'^{^\eta} \quad (85)$$

Viscous Flux

Viscous terms are discretized using a non-upwind fluctuation splitting formulation, which is equivalent to a finite element discretization using mass-lumping to the nodes. Both the finite volume and the upwind fluctuation splitting inviscid discretizations have been shown by the authors[13] to be compatible with this viscous treatment for scalar equations.

Integrating the viscous flux over a triangular element leads to the viscous fluctuation,

$$\boldsymbol{\phi}^v = \int_\Omega \vec{\nabla}\cdot(\varpi_a \vec{\mathbf{F}}^v)\, d\Omega \quad (86)$$

The nodal distributions are developed in a finite element sense by integrating by parts,

$$\boldsymbol{\phi}_i^v = \oint_\Gamma \upsilon_i \varpi_a \vec{\mathbf{F}}^v \cdot \hat{n}\, d\Gamma - \int_\Omega \varpi_a \vec{\mathbf{F}}^v \cdot \vec{\nabla}\upsilon_i\, d\Omega \quad (87)$$

For interior nodes the boundary integral in Eqn. 87 will sum to zero and the volume integral is integrated analytically for a linear variation of the parameter vector,

$$\vec{\nabla}\mathbf{Z} = -\frac{1}{2S_\mathsf{T}} \sum_{j=1}^{3} \mathbf{Z}_j \ell_j \hat{n}_j \qquad \vec{\nabla}\upsilon_i = -\frac{\ell_i \hat{n}_i}{2S_\mathsf{T}} \quad (88)$$

$$\boldsymbol{\phi}_i = \frac{\ell_i}{2S_\mathsf{T}} \int_\Omega \varpi_a \vec{\mathbf{F}}^v \cdot \hat{n}_i\, d\Omega = \frac{\bar{\varpi}_a \ell_i}{2} \tilde{\vec{\mathbf{F}}}^v \cdot \hat{n}_i \quad (89)$$

Struijs *et al*[14] have shown that derivatives of primitive variables can be consistently represented in terms of the parameter vector gradients as,

$$\widetilde{\vec{\nabla}\mathbf{V}} = \mathbf{V}_{\bar{Z}}\, \vec{\nabla}\mathbf{Z} \quad (90)$$

where,

$$\mathbf{V}_Z = \begin{bmatrix} 2Z_1 & 0 & 0 & 0 \\ -\frac{Z_2}{Z_1^2} & \frac{1}{Z_1} & 0 & 0 \\ -\frac{Z_3}{Z_1^2} & 0 & \frac{1}{Z_1} & 0 \\ \frac{\gamma-1}{\gamma} Z_4 & -\frac{\gamma-1}{\gamma} Z_2 & -\frac{\gamma-1}{\gamma} Z_3 & \frac{\gamma-1}{\gamma} Z_1 \end{bmatrix} \quad (91)$$

and,

$$\tilde{\mathbf{V}} = \mathbf{V}(\bar{\mathbf{Z}}) = \begin{pmatrix} \bar{Z}_1^2 \\ \frac{\bar{Z}_2}{\bar{Z}_1} \\ \frac{\bar{Z}_3}{\bar{Z}_1} \\ \frac{\gamma-1}{\gamma}\left[\bar{Z}_1\bar{Z}_4 - \frac{1}{2}\left(\bar{Z}_2^2 + \bar{Z}_3^2\right)\right] \end{pmatrix} \quad (92)$$

Further, the consistent temperature gradient is,

$$\widetilde{\vec{\nabla}T} = \frac{\widetilde{\vec{\nabla}P}}{\tilde{\rho}R} - \frac{\tilde{P}\widetilde{\vec{\nabla}\rho}}{\tilde{\rho}^2 R} = \frac{1}{R\tilde{\rho}^2}\left(\tilde{\rho}\widetilde{\vec{\nabla}P} - \tilde{P}\widetilde{\vec{\nabla}\rho}\right) \quad (93)$$

The viscous fluctuation is then distributed to the nodes,

$$S_i\mathbf{U}_{i_t} \leftarrow \boldsymbol{\phi}_i^v + COE \quad (94)$$

An alternate approach to integrating the viscous flux is obtained by using the divergence theorem,

$$\int_{\Omega_i} \vec{\nabla}\cdot(\varpi_a \vec{\mathbf{F}}^v)\, d\Omega = \oint_{\Gamma_i} \varpi_a \vec{\mathbf{F}}^v \cdot \hat{n}\, d\Gamma \quad (95)$$

where Ω_i is the generalized control volume containing node i, with two-dimensional area equal to S_i, and Γ_i is the boundary of Ω_i.

Haselbacher *et al*[12] have recently presented an approximate treatment for integrating Eqn. 95 on two-dimensional unstructured grids, which they relate to the thin-layer approximation of the Navier-Stokes equations presented by Gnoffo[15] for structured grids. The method preserves positivity for the Laplacian and is transparent to grid topology.

The development begins with the expression,

$$\vec{\mathbf{F}}^v \cdot \hat{n} = \frac{1}{R_{e_\infty}} \begin{pmatrix} 0 \\ \mu \left[\vec{\nabla} u \cdot \hat{n} + \frac{1}{3} \vec{\nabla} \cdot \vec{V} n^{\mathrm{x}} - \vec{\nabla} v \cdot \hat{t} \right] \\ \mu \left[\vec{\nabla} v \cdot \hat{n} + \frac{1}{3} \vec{\nabla} \cdot \vec{V} n^{\mathrm{y}} + \vec{\nabla} u \cdot \hat{t} \right] \\ \kappa \vec{\nabla} T \cdot \hat{n} + \mu \left[\frac{1}{3} (\vec{\nabla} \cdot \vec{V}) (\vec{V} \cdot \hat{n}) \right. \\ \left. + \frac{1}{2} \vec{\nabla} V^2 \cdot \hat{n} - u \vec{\nabla} v \cdot \hat{t} + v \vec{\nabla} u \cdot \hat{t} \right] \end{pmatrix} \quad (96)$$

where $\hat{t}$ is a tangent vector with components $(-n^{\mathrm{y}},\ n^{\mathrm{x}})$. Haselbacher's approximation neglects all tangential terms and approximates $\vec{\nabla} \cdot \vec{V} \simeq n^{\mathrm{x}} \vec{\nabla} u \cdot \hat{n} + n^{\mathrm{y}} \vec{\nabla} v \cdot \hat{n}$. Using the notation $u_n = \vec{\nabla} u \cdot \hat{n}$, etc., and including the axisymmetric terms gives the approximation,

$$\vec{\nabla} \cdot \vec{V} \simeq \vec{V}_n \cdot \hat{n} + \varpi \frac{v}{y} \quad (97)$$

leading to,

$$\vec{\mathbf{F}}^v \cdot \hat{n} \simeq \frac{\mu}{R_{e_\infty}} \begin{pmatrix} 0 \\ \vec{V}_n^{\mathsf{T}} + \frac{1}{3} \hat{n}^{\mathsf{T}} \left(\vec{V}_n \cdot \hat{n} + \varpi \frac{v}{y} \right) \\ \frac{\kappa}{\mu} T_n + \vec{V} \cdot \vec{V}_n + \frac{1}{3} \vec{V} \cdot \hat{n} \left(\vec{V}_n \cdot \hat{n} + \varpi \frac{v}{y} \right) \end{pmatrix} \quad (98)$$

A further simplification aligns $\hat{n}$ with the nearest mesh edge for faces of Γ on the interior of the domain, so that terms such as u_n reduce simply to the difference in nodal values divided by edge length. Also, ϖ_a is chosen to be the midpoint of the edge.

Including one more approximation, namely replacing the length Γ of the median-dual face with the length of the associated containment-dual face, has the effect of canceling some of the errors for very high-aspect-ratio cells introduced by assuming $\hat{n}$ is edge-aligned. For low-aspect-ratio cells, the containment dual is the same as the median dual and the true $\hat{n}$ is closely aligned with the mesh edge. This implementation is similar to the suggestions of both Barth[6] and Haselbacher,[16] yet retains the global median-dual implementation required by a distribution scheme.

Boundary Conditions

Boundary nodes may be updated either strongly, where the nodal solution values are simply assigned *a priori*, or weakly, where the solution values at the boundary nodes are relaxed in time using the same formulations as for interior nodes.

For finite volume, the weak boundary implementation specifies the solution state to the outside of boundary faces, then allows the approximate Riemann solver to construct the appropriate fluxes through the boundary faces. See Figure 3 for an illustration of the weak finite volume boundary condition. The solution state to the inside of the boundary face can be set from either a first- or second-order reconstruction from the

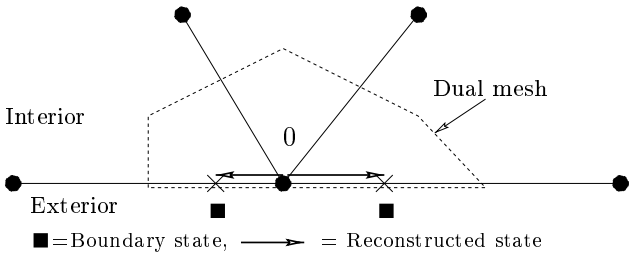

Fig. 3 Weak implementation of finite volume boundary condition for node 0, imposed by specifying external state. Quadrature points denoted by X's.

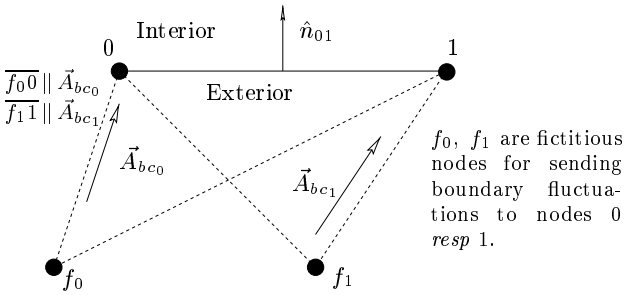

Fig. 4 Weak implementation of fluctuation splitting boundary condition, imposed by specifying external state at ghost nodes $f_0,\ f_1$.

node. For some cases, second-order reconstruction to boundary faces has led to localized oscillations in the solution convergence at boundary nodes.

Weak formulation of the fluctuation splitting boundary condition is developed using fictitious "ghost" nodes, one for each boundary node, as shown in Figure 4. Considering the scalar case, the positioning of a ghost node such that the edge connecting the ghost and boundary nodes is parallel to the advection velocity results in a boundary fluctuation of,

$$\phi_{bc_0} = \frac{1}{2} \ell_{01} \vec{A} \cdot \hat{n}_{01} (U_{f_0} - U_0) \quad (99)$$

for node 0 of Figure 4. Observe that this formulation is independent of the physical location of the ghost node, so the ghost node can be chosen to be infinitesimally close to the boundary node it supports. The solution state at the ghost node remains to be specified, and can be varied node-to-node. The associated artificial dissipation is,

$$\phi'_{bc_0} = \mathrm{sign}(\vec{A} \cdot \hat{n}_{01}) \phi_{bc_0} \quad (100)$$

and the resulting distribution is,

$$S_0 U_{0_t} \leftarrow \frac{1}{2} (\phi_{bc_0} + \phi'_{bc_0}) + COE \quad (101)$$

Since no account of the ghost cell area is made in forming the dual area on the LHS of Eqn. 101, a scale factor on $[\frac{1}{2}, 1]$ can be applied to the distribution.

The extension to systems follows by analogy. The boundary fluctuation is defined,

$$\breve{\phi}_{bc_0} = \frac{\varpi_{a_0}}{2}\ell_{01}\vec{\mathcal{A}}_{bc_0}\cdot\hat{n}_{01}(\mathbf{W}_{f_0}-\mathbf{W}_0) \tag{102}$$

with the artificial dissipation,

$$\breve{\phi}'_{bc_0} = \text{sign}(\vec{\mathcal{A}}_{bc_0}\cdot\hat{n}_{01})\breve{\phi}_{bc_0} \tag{103}$$

Additional dissipation for the suppression of expansion shocks is added to Eqn. 103 following the form of Eqns. 80 and 81 as,

$$+\varpi_{a_0}\frac{\ell_{01}}{2}\begin{bmatrix} 0 & 0 & 0 & 0 \\ 0 & n_{01}^{x^2}\delta^+ & n_{01}^x n_{01}^y\delta^+ & \frac{n_{01}^x}{a}\delta^- \\ 0 & n_{01}^x n_{01}^y\delta^+ & n_{01}^{y^2}\delta^+ & \frac{n_{01}^y}{a}\delta^- \\ 0 & an_{01}^x\delta^- & an_{01}^y\delta^- & \delta^+ \end{bmatrix} \cdot(\mathbf{W}_{f_0}-\mathbf{W}_0) \tag{104}$$

The distribution to the boundary node is then formed as,

$$S_0\mathbf{U}_{0_t} \leftarrow \frac{1}{2}\mathbf{U}_W(\breve{\phi}_{bc_0}+\breve{\phi}'_{bc_0})+COE \tag{105}$$

This system treatment is only approximate, as the cross-fluctuation does not vanish when $\vec{V}\parallel\overline{f_0 0}$, as in the scalar case, but reduces to the term,

$$\begin{bmatrix} 0 & 0 & 0 & 0 \\ 0 & 0 & 0 & n_{f_0}^x \\ 0 & 0 & 0 & n_{f_0}^y \\ 0 & a^2 n_{f_0}^x & a^2 n_{f_0}^y & 0 \end{bmatrix} \tag{106}$$

Strictly, there should be some cross-coupling with the neighboring boundary nodes. However including the term from Eqn. 106 requires explicitly locating the ghost nodes, which can be impossible for certain geometries.

The distribution to node 1 is formed analogously, substituting 0 for 1 in Eqns. 99–106.

The freestream boundary condition is enacted by specifying a complete, constant thermodynamic state and velocity vector. By using the weak boundary enforcement, this one boundary condition covers the four permutations of subsonic or supersonic, inflow or outflow.

The inviscid wall boundary is implemented by mirroring the primitive variables, either across the face for finite volume or at the node for fluctuation splitting.

The axisymmetric axis is enforced by imposing zero flux on the axis and using the control-volume centroid for $\overline{\varpi}_a$ in Eqn. 8.

Viscous walls define a stagnant velocity and a specified wall temperature. The zero velocity at the wall causes the viscous axisymmetric source to be zero.

Both the full viscous flux and the approximate thin-layer flux of Haselbacher reduce to,

$$\vec{\mathbf{F}}^v\cdot\hat{n} = \frac{1}{R_{e_\infty}}\left[0,\ \mu\vec{V}_n,\ \kappa T_n\right] \tag{107}$$

at a wall, since $\vec{V}$, $\vec{\nabla}\vec{V}$, and $\vec{V}_n\cdot\hat{n}$ go to zero. Defining the heat transfer into the wall according to Fourier's law,

$$q_w = -\frac{\kappa}{R_{e_\infty}}T_n \tag{108}$$

and the wall shear stress,

$$\vec{\tau}_w = -\frac{\mu}{R_{e_\infty}}\vec{V}_n \tag{109}$$

allows the Eqn. 107 to be written as,

$$\vec{\mathbf{F}}^v\cdot\hat{n} = -\left[0,\ \vec{\tau}_w,\ q_w\right] \tag{110}$$

where the minus sign results from the choice of an outward unit normal, $\hat{n}$, to the control volume, which points into the wall at a boundary.

The solid wall is enforced weakly, by specifying the wall shear that will drive the flow momentum to zero and the heat flux that will drive the solution temperature to the desired wall temperature. An advantage of this weak approach is that wall heat transfer and skin friction are solved for directly, rather than as a post-processed least-squares reconstruction. Using an explicit update, the wall heat flux can be isolated as,

$$q_w = \frac{1}{\varpi_a\sum\Gamma_w}\left[\frac{\varpi_a S}{\Delta t}\left(U_4 - U_1\, e(T_w)\right)+RHS_4^{i+v}\right] \tag{111}$$

Similarly, the wall shear is,

$$\vec{\tau}_w = \frac{1}{\varpi_a\sum\Gamma_w}\left[\frac{\varpi_a S}{\Delta t}(U_2,U_3)+RHS_{2,3}^{i+v}\right] \tag{112}$$

Temporal Evolution

Solutions at the nodes are updated using an explicit forward-Euler LHS. A Jacobi relaxation strategy is followed with either local time stepping or first-order global time steps.

The CFL (Courant *et al*[17]) criteria for explicit schemes is adapted for use with the node-based unstructured scheme. The inviscid timestep is defined by the most restrictive time for signal propagation, at the eigen-value speeds, between adjacent nodes,

$$\Delta t_0 = \min\left(\frac{\|\vec{r}_{0i}\|}{|\vec{V}_0\cdot\hat{r}_{0i}|+a_0}\right)=\min\left(\frac{\vec{r}_{0i}\cdot\vec{r}_{0i}}{|\vec{V}_0\cdot\vec{r}_{0i}|+a_0\|\vec{r}_{0i}\|}\right) \tag{113}$$

where the current node is node 0 and i takes on nodal values for each distance-one neighbor of the current node.

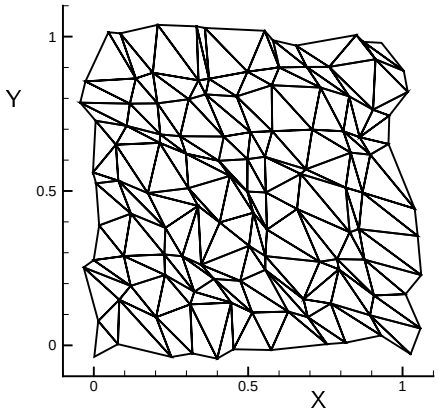

Fig. 5 Sample randomly distorted mesh used for solver verification cases.

The viscous timestep restriction is taken to be an approximation based upon the positivity analysis for the scalar case,[13] assuming order-1 Prandtl number,

$$\Delta t_0 = \frac{4 S_0 \rho_0 R_{e_\infty} R}{\mu_0 (R + \gamma - 1) \sum_{\mathsf{T}} \frac{\ell_0^2}{S_{\mathsf{T}}}} \qquad (114)$$

The stability and convergence of axisymmetric solutions is found to be enhanced by scaling the timestep for points near the cylindrical axis by the maximum of either the node height or the square root of the median-dual area.

The more restrictive of the inviscid or viscous timestep is used to scale the nodal update.

Results

Verification of the complete solver is performed in stages using a methodology derivative of Singhal.[1] A variety of canonical cases are constructed, including grid distortions, that are designed to exercise combinations of the various functions that comprise the complete solver. Two viscous cases serve to validate the solver against benchmark data.

Inviscid Verification

Distorted mesh

The first verification case simply passes a uniform flow through a distorted grid, with success being the preservation of uniformity to at least six significant digits. The domain is initialized to stagnant conditions with freestream flow impulsively applied at the boundaries. A variety of flow angles were tested on $-180° \leq \text{AOA} \leq 180°$ for subsonic, transonic, and supersonic Mach numbers. Regular, high aspect ratio (100), skewed ($2° < \theta < 175°$), and randomly distorted (Figure 5) meshes with 121 nodes were used. Initial runs were instrumental in refining the treatment of eigen-value limiting for fluctuation splitting.

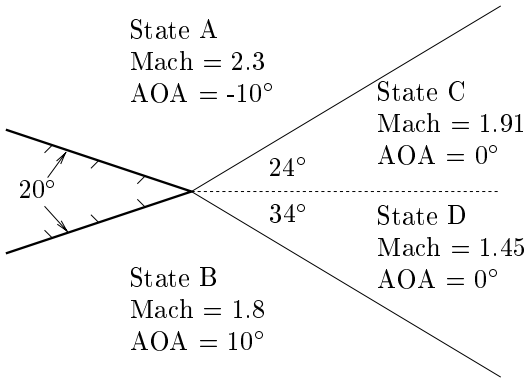

Fig. 6 Description of converging-Mach-stream problem. Flow from left to right, with oblique shocks, solid, and slip-line, dashed, emanating from trailing edge of splitter plate.

All final runs were successful for both finite volume and fluctuation splitting.

Converging Mach streams

Thermodynamic routines are verified by considering converging Mach streams, inclined at $\pm 10°$. The upper stream is at Mach 2.3 while the lower stream has Mach 1.8. The two streams have matched densities but a temperature ratio of 1.0812, resulting in a horizontal slip line behind the oblique shocks. A complete description of the analytic solution appears in Figure 6 and Table 1.

A sequence of four meshes, with a refinement ratio of 1.5, is considered. The meshes are triangulated from 16×16, 24×24, 36×36, and 54×54 grids. The triangulated 16×16 grid is shown in Figure 7. The finer meshes cover the same domain and are constructed similarly to the shown mesh.

A Mach-number contour plot for fluctuation splitting on the finest mesh is shown in Figure 8, showing crisp discontinuity resolution and the correct post-shock Mach numbers. The shock angles for all eight cases, *i.e.* finite volume and fluctuation splitting on each mesh, are measured to be correct within $\pm 1°$. The L_2-norms of the primitive-variables error at states C and D are plotted versus the characteristic mesh size in Figure 9. The slopes of the regression lines are indicative of the order of accuracy with respect to grid convergence of the two schemes for this test case.

Table 1 Analytic thermodynamic states for converging Mach streams.

State	ρ, kg/m^3	T, K	P, kPa	V, m/s
A	1.2	300	103.34	798.6
B	1.2	324.7	111.73	649.9
C	1.813	356.7	185.62	723.7
D	1.718	376.4	185.62	563.7

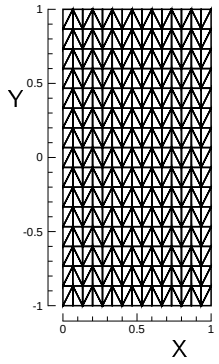

Fig. 7 16×16 **mesh for converging Mach streams.**

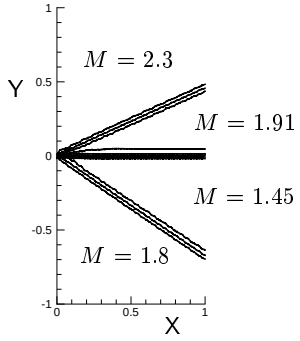

Fig. 8 Mach contours from fluctuation splitting on finest mesh.

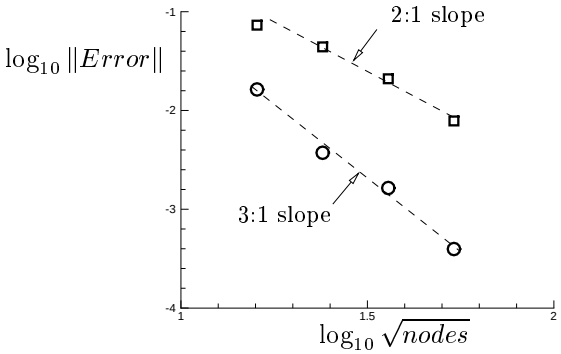

Fig. 9 Grid convergence rates for converging Mach stream case. Circles = fluctuation splitting, squares = finite volume.

Finite volume exhibits second-order convergence, as expected. Unexpectedly, fluctuation splitting shows super-convergence for this particular case. True multi-dimensional upwinding is likely the source of the exceptional fluctuation splitting accuracy for this purely-supersonic flow. Supplementing the graphical determination of the grid-convergence rates, the equations presented by Roache,[2] based on a Richardson extrapolation, yield average grid-convergence rates of 3.0 for

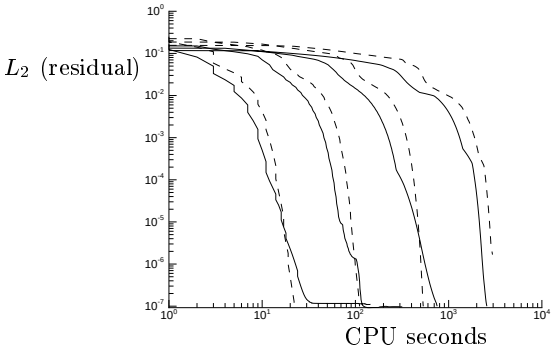

Fig. 10 Convergence histories for converging Mach-stream case. Fluctuation splitting solid, finite volume dashed. Coarsest mesh on left, finest on right.

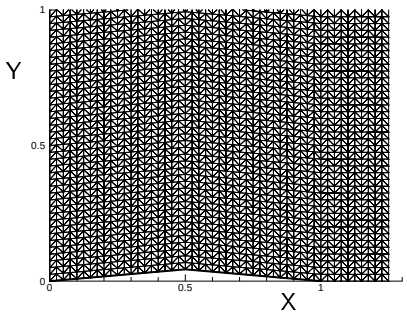

Fig. 11 Grid for diamond airfoil verification test.

fluctuation splitting and 2.1 for finite volume.

Temporal convergence rates are plotted in Figure 10, with timings performed on an IRIS R10000 platform. All cases were run using the Minmod limiter and a Jacobi update strategy with local time steps. Fluctuation splitting was run with a unity CFL number, while best convergence for finite volume was found for CFL=0.7. Fluctuation splitting runs at 145 μs per node per iteration, while finite volume runs at 165 μs per node per iteration.

Diamond airfoil

A verification of the inviscid wall boundary condition is performed on a diamond airfoil at zero angle of attack and Mach 1.5. The flow deflection is five degrees. The grid is shown in Figure 11. A Mach-number contour plot using fluctuation splitting is shown in Figure 12. The corresponding finite volume solution, not shown, is visually indistinguishable from the fluctuation splitting solution. The analytic drag coefficient, based on chord length, is 0.02760. The fluctuation splitting drag coefficient is 0.02638, for a 4.4 percent error. The finite volume result has an error of 6.6 percent from a drag coefficient of 0.02579.

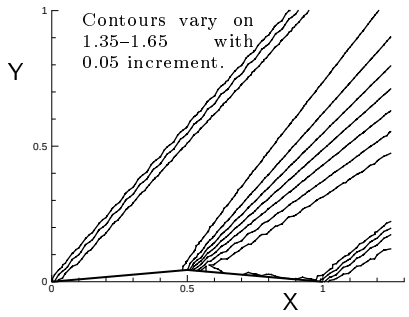

Fig. 12 Mach contours on diamond airfoil, $M = 1.5$, fluctuation splitting solution.

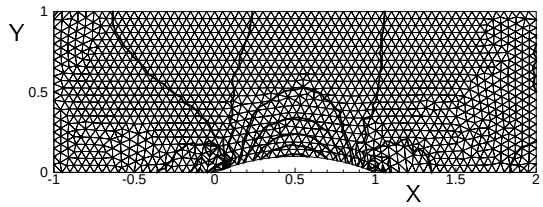

Fig. 13 Two-dimensional 10 percent circular-bump mesh with isobars from fluctuation splitting solution at Mach 0.1.

Circular bump

A subsonic two-dimensional verification is performed on a 10 percent circular bump at Mach 0.1. The 1389-node mesh with isobars from the fluctuation splitting solution is shown in Figure 13. A true incompressible inviscid flow would have symmetric isobars fore and aft, and zero drag. The fluctuation splitting drag coefficient, based on cord length is 0.0058. Finite volume predicts a drag coefficient more than twice as large, 0.0128. A lower fluctuation splitting drag coefficient is indicative of lower levels of artificial dissipation in the solution for this case.

Sphere

In a similar vein, Mach 0.1 axisymmetric flow over a sphere is tested on a 1369-node mesh. The drag coefficient, based on frontal area, is 0.43 for finite volume but 0.56 for fluctuation splitting. Contrary to expectation, the increased artificial dissipation in the finite volume solution creates enough of a total pressure loss to nearly eliminate separation on the leeside, whereas the leeside increase in pressure toward the centerline in the fluctuation splitting solution does produce a sizable separation region, and in this case a larger drag coefficient. As with subsonic bump case, true incompressible, inviscid flow should theoretically produce zero drag.

Cone

The final inviscid verification is for an 11-degree semi-vertex-angle cone at Mach 1.5. The well-established Taylor-Maccoll[18] method for the conical supersonic Euler equations predicts a drag coefficient, based on base area with no base pressure, of 0.7795. The fluctuation splitting solution, which converged seven orders of magnitude in 38 seconds, predicts a drag coefficient of 0.7785, for only a 0.13 percent error. The finite volume solution, which took 13 percent longer at 43 seconds to reach seven orders of magnitude residual convergence, predicts a 0.7754 coefficient, for an error of 0.53 percent.

Viscous Validation

Two canonical viscous validation cases are considered: a subsonic flat plate and a hypersonic cylinder. Steady laminar solutions are obtained using the Haselbacher thin-layer viscous treatment with containment-dual modification.

Flat plate

The classic Blasius[19] flat-plate boundary layer problem is solved on a rectangular domain. Mach 0.3 flow enters 2 units upstream of the plate leading edge, which is located at the origin. The plate is 4 units long, ending at an extrapolation outflow boundary. The upper boundary is 1.2 units above the plate. The Reynolds number is 10^4.

The meshes are obtained from a structured grid containing 37 equally-spaced points parallel to the plate, 12 points upstream of the plate and 25 points on the plate, and 41 points normal to the plate. The vertical grid spacing at the wall is 0.001 units with an exponential stretching as described in Ref. 20, placing approximately 20 nodes within the boundary layer. The unstructured mesh is formed from the structured grid using diagonal cuts in an alternating pattern. Two coarser meshes are similarly constructed by successively deleting every-other node in the wall-normal direction, leaving 10 and 5 nodes, respectively, in the boundary layer for the medium and coarse grids.

Boundary layer profiles of u are extracted at $x = 1, 2, 3$ from both the fluctuation splitting and finite volume solutions and plotted versus the Blasius solution in Figure 14. The boundary layer scaling variable is defined as,

$$\eta = y\sqrt{\frac{R_e}{x}} \tag{115}$$

Both solution sets match the Blasius profile, indicating well-developed flow with adequate grid resolution on the finest mesh.

Figure 15 shows the effect of using the containment-dual approximation in the Haselbacher thin-layer viscous treatment. Boundary layer profiles of u are again extracted at $x = 1, 2, 3$, with both solutions being run with fluctuation splitting. Figure 15(a) is the same

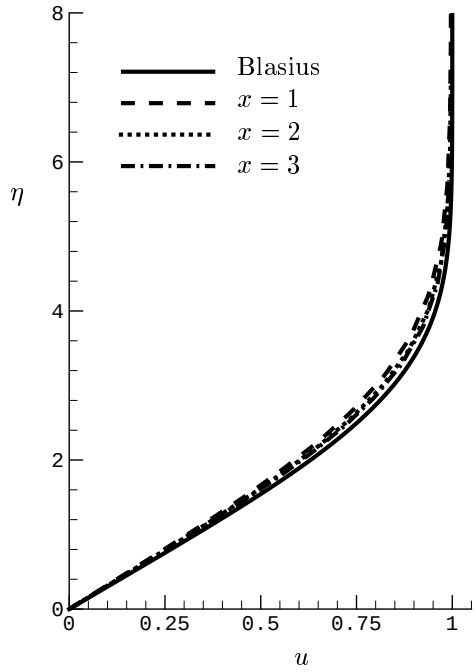

a) Fluctuation splitting.

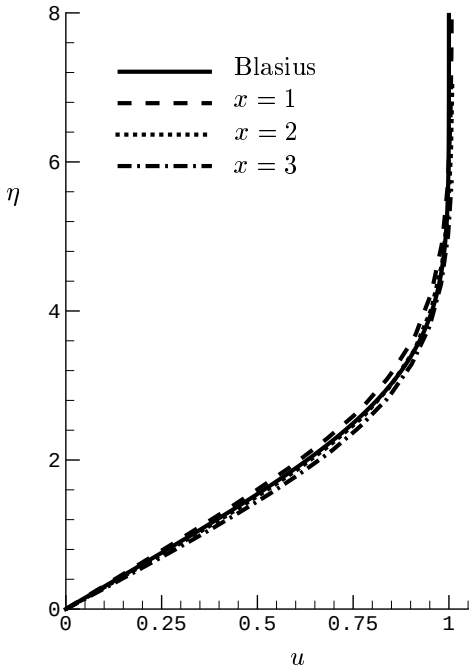

b) Finite volume.

Fig. 14 Boundary layer profiles of tangential velocity extracted from three stations on flat plate.

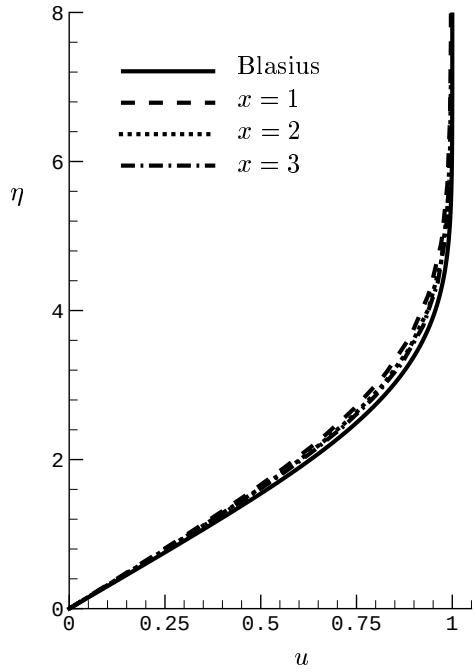

a) Containment dual approximation.

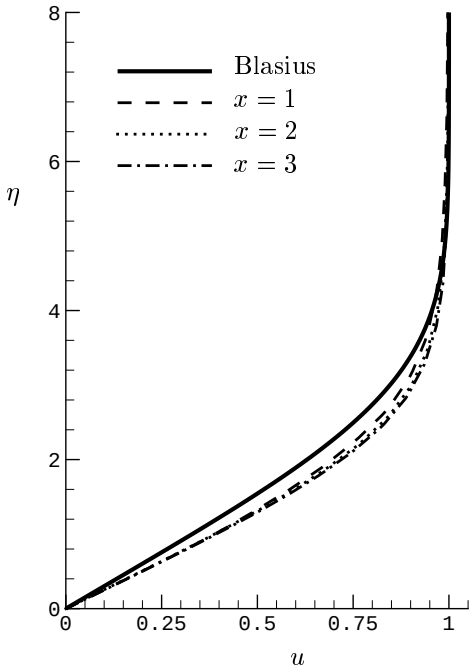

b) Strict median dual implementation.

Fig. 15 Boundary layer profiles computed using two different viscous dual mesh definitions.

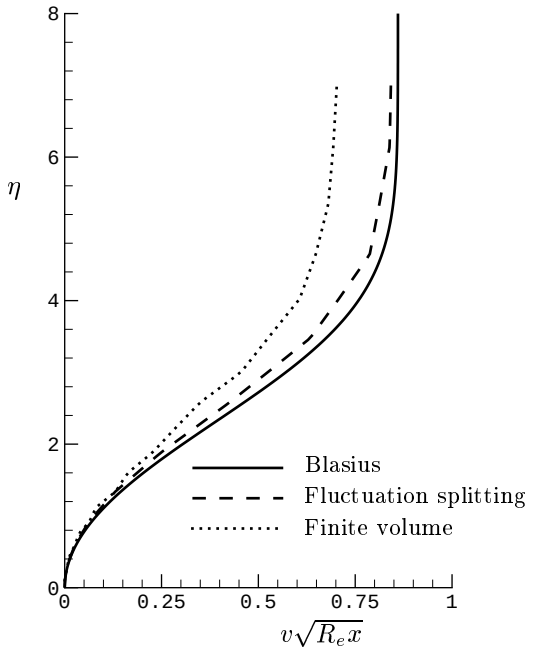

Fig. 16 Boundary layer profiles of vertical velocity extracted from midpoint of flat plate.

as Figure 14(a), while Figure 15(b) uses the strict median-dual definition for the viscous terms. For the highly-stretched grid elements used in this case, it is clear that the containment-dual approximation provides improved boundary-layer resolution, while omitting the approximation leads to a profile that is "too full."

The v-velocity profiles from the fluctuation splitting and finite volume solutions are compared in Figure 16, both extracted from the plate at $x = 2$. The fluctuation splitting solution comes much closer to matching the Blasius profile than the finite volume result. Excessive artificial dissipation is produced by the finite volume scheme in the y-momentum equation, which suppresses the v-velocity below the analytic value. The artificial dissipation contributions to the y-momentum equation are plotted for both fluctuation splitting and finite volume in Figure 17. The vertical scale has been enlarged by a factor of 30 to zoom in on the boundary layer in Figure 17. Clearly, finite volume is producing significantly more artificial dissipation than fluctuation splitting over the length of the boundary layer.

For this essentially incompressible case, the suppression of the vertical velocity due to excessive artificial dissipation is manifested by an increase in skin friction coefficient, as shown in Figure 18, where the friction coefficient increases with running length for finite volume, but not for fluctuation splitting. Recall that finite volume is continuously producing artificial dissipation over the length of the plate while the fluctuation splitting dissipation is restricted to the leading-edge region only. Figure 18 presents data from all three

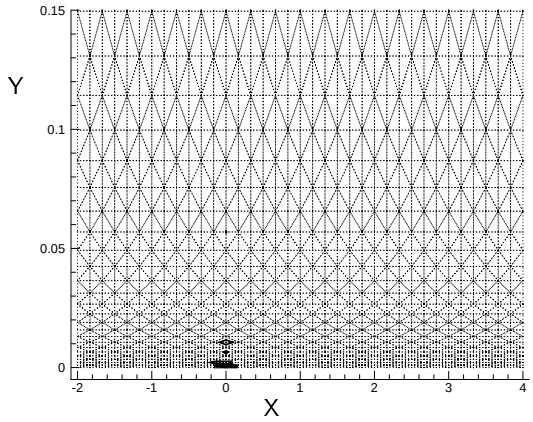

a) Fluctuation splitting.

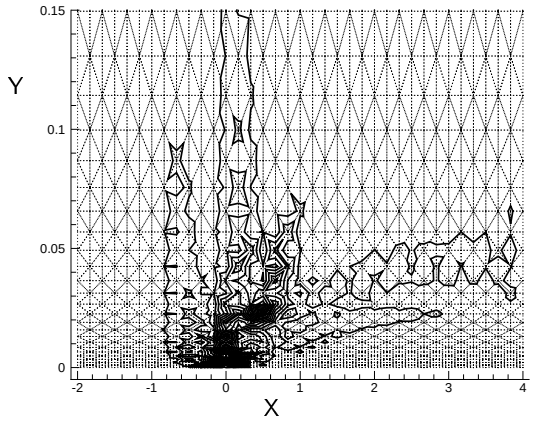

b) Finite volume.

Fig. 17 Artificial dissipation production in the y-momentum equation. Eleven contours spaced equally on 0–0.0005.

grid refinement levels. The finite volume results degrade dramatically with coarsening of the mesh, but the fluctuation splitting results remain relatively invariant with mesh resolution, all the way down to only five nodes in the boundary layer.

The medium-mesh finite volume solution was repeated using the full Navier-Stokes treatment, rather than the thin-layer equations. No change in the skin-friction results are seen over the first half of the plate, Figure 19, though there is an 8-percent improvement toward the end of the plate. Solving for the full Navier-Stokes terms requires 11 percent more CPU time per iteration.

Cylinder

The opposite end of the Mach-number spectrum is used to validate heat-transfer calculations, in this case for a cylinder of 1 m radius in Mach 17.6 flow. The perfect-gas assumption is a poor physical model for these extreme conditions, $V_\infty = 5$ km/s, $\rho_\infty = 0.001$ kg/m^3, $T_\infty = 200$ K, $T_{wall} = 500$ K, but the

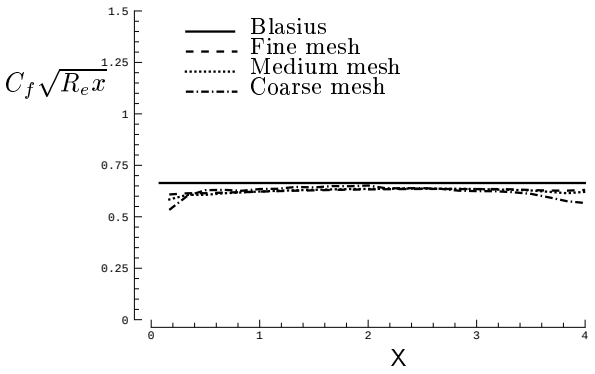

a) Fluctuation splitting.

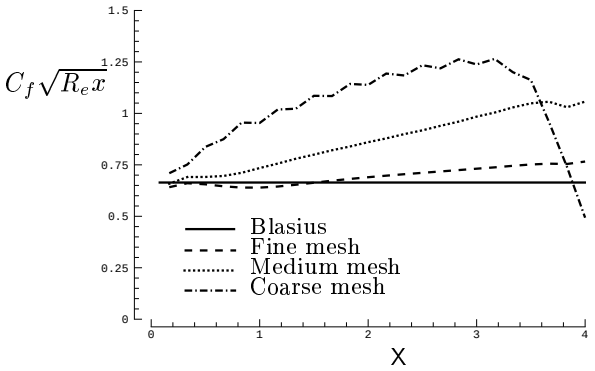

b) Finite volume.

Fig. 18 Skin friction coefficients for Blasius flow.

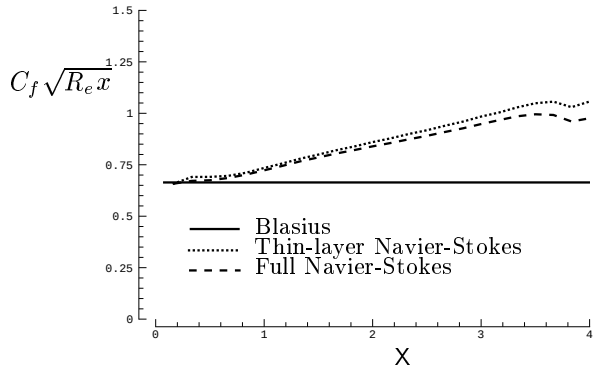

Fig. 19 Effect of viscous modeling on skin friction.

case provides a severe test of the algorithms under a re-entry scenario. Results are compared against the LAURA[15,21,22] benchmarks.* The LAURA code is well-established as a structured-grid hypersonic solver. Also included in the LAURA benchmark data is a solution using the unstructured-mesh finite volume solver FUN2D.[23] The unstructured grid for this case was obtained by simple triangulation of the LAURA grid, which has 65 nodes perpendicular to the surface, clustered to the wall, and circumferential nodes spaced every 3 degrees. Only the forward-half of the cylinder is solved, as shown in the mesh and flowfield solution of Figure 20.

The surface pressure coefficient is plotted versus rotation angle from the stagnation point for both the fluctuation splitting and finite volume solutions, along with the LAURA and FUN2D results in Figure 21. The LAURA, FUN2D, and fluctuation splitting curves all over-plot, and the finite volume solution nearly over-plots, being 1 percent low at the stagnation point and slightly high by a similar amount 90 degrees away. The calculations were repeated on a grid coarsened by a factor of four (skip of two in both structured-grid directions), with surface pressure results plotted in Figure 22 along with the fine-mesh LAURA solution. The coarsened fluctuation splitting surface pressures retain good agreement, and the finite volume solution matches over most of the cylinder, with minor exceptions again at the stagnation point, 1 percent high on this grid, and at the 90 degree point.

Surface heat-transfer rates for LAURA, FUN2D, and fluctuation splitting are shown in Figure 23. Both of the unstructured-mesh solutions show elevated heating at the stagnation region, with fluctuation splitting being 30 percent higher than LAURA while FUN2D is 50 percent higher. Heating results for this case were also obtained using a validated structured-mesh coupled inviscid/boundary-layer code, with the solution agreeing with the LAURA data.

The fine-mesh solutions were repeated using the full Navier-Stokes treatment, and no changes in heating levels were observed.

Concluding Remarks

A multi-dimensional upwind fluctuation splitting scheme has been formulated for two-dimensional/axisymmetric viscous flows. A weak form of the boundary conditions was proposed and the proper incorporation of eigen-value limiting derived.

While the scheme is formally second-order accurate, super-convergent third-order behavior was seen for a canonical verification test of converging supersonic streams.

The fluctuation splitting scheme produced more accurate solutions for the inviscid diamond airfoil and circular bump than a finite volume scheme. Paradoxically, the excessive artificial dissipation produced by the finite volume scheme actually led to a lower drag than fluctuation splitting for the subsonic inviscid sphere case.

For the viscous flat plate, fluctuation splitting was seen to produce more accurate solutions than finite volume, due to the fluctuation splitting low levels of artificial dissipation. Also, fluctuation splitting showed excellent skin-friction predictions on extremely coarse meshes, while the finite volume results deteriorated

*`http://hefss.larc.nasa.gov`

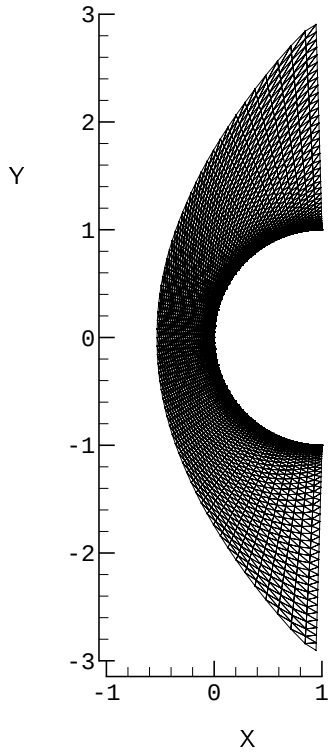

a) Grid.

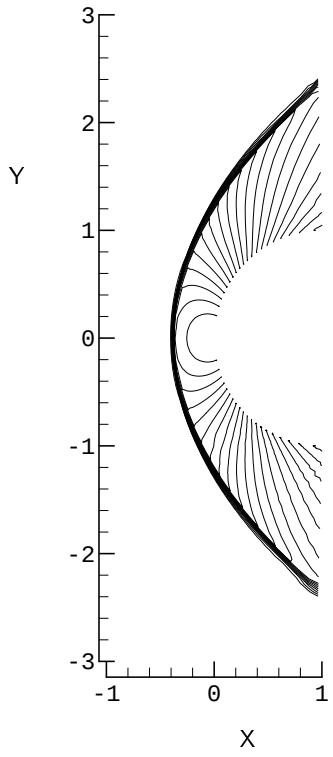

b) Pressure contours.

Fig. 20 Hypersonic cylinder domain with fluctuation splitting solution.

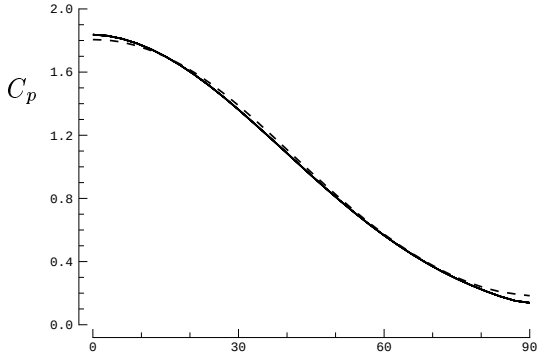

Fig. 21 Cylinder surface pressures, solid = fluctuation splitting, LAURA, and FUN2D, while dashed = finite volume.

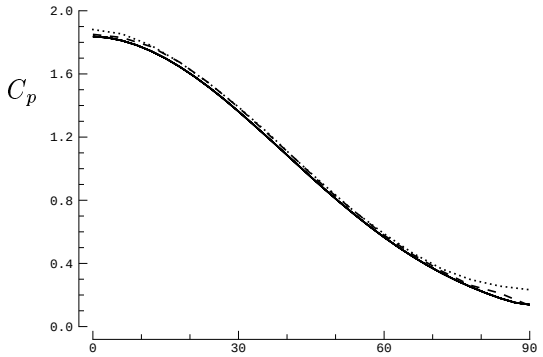

Fig. 22 Cylinder surface pressures on coarsened mesh, solid = LAURA, dashed = fluctuation splitting, and dotted = finite volume.

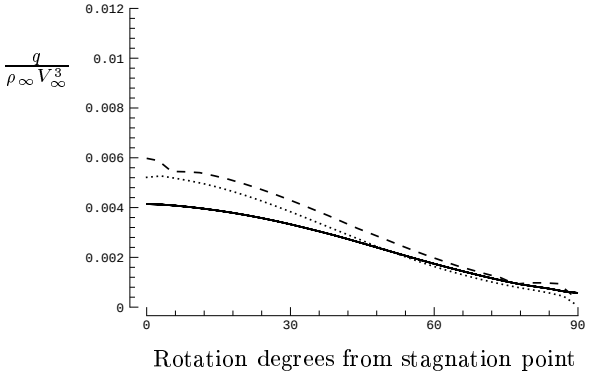

Fig. 23 Cylinder surface heat-transfer rates, solid = LAURA, dashed = FUN2D, and dotted = fluctuation splitting.

with mesh coarsening.

Surface pressures were well predicted for the hypersonic viscous cylinder, but surface heating was disappointingly high for all the unstructured schemes considered here relative to the benchmark solution. Further testing is warranted to probe the validity of unstructured meshes for hypersonic viscous solutions. Mixed-element strategies may be a more-appropriate course for high-Mach-number applications, with the fluctuation splitting inviscid distribution assigned from an implicit triangulation in the boundary layer.

Therefore, the upwind fluctuation splitting inviscid discretization is an attractive solver from subsonic through hypersonic regimes *vis a vis* finite volume for a fresh code build, but the benefits are perhaps not great enough to justify rebuilding a legacy code. However, when coupled with a viscous discretization the reduced levels of artificial dissipation in fluctuation splitting allow for coarser viscous meshes, which can lead to significantly reduced computational requirements.

Acknowledgments

The inviscid/boundary layer solution for the cylinder case was provided by H. Harris Hamilton, II of NASA Langley Research Center.

References

[1]Shinghal, A. K., "Key Elements of Verification and Validation of CFD Software," AIAA Paper 98–2639, June 1998.

[2]Roache, P. J., "Verification of Codes and Calculations," *AIAA J.*, Vol. 36, No. 5, May 1998, pp. 696–702.

[3]Navier, M., "Mémoire sur les lois du Mouvement des Fluides," *Mémoire de l'Académie des Sciences*, Vol. 6, 1827, pp. 389.

[4]Stokes, G. G., "On the Theories of the Internal Friction of Fluids in Motion," *Trans. Cambridge Philosophical Society*, Vol. 8, 1849, pp. 227–319.

[5]Barth, T. J. and Jesperson, D. C., "The Design and Application of Upwind Schemes on Unstructured Meshes," AIAA Paper 89–0366, Jan. 1989.

[6]Barth, T. J., "Aspects of Unstructured Grids and Finite-Volume Solvers for the Euler and Navier-Stokes Equations," *Computational Fluid Dynamics*, No. 1994–04 in Lecture Series, von Karman Institute for Fluid Dynamics, 1994.

[7]Sidilkover, D., "A Genuinely Multidimensional Upwind Scheme and Efficient Multigrid Solver for the Compressible Euler Equations," Report 94–84, ICASE, USA, Nov. 1994.

[8]Sidilkover, D. and Roe, P. L., "Unification of Some Advection Schemes in Two Dimensions," Report 95–10, ICASE, Hampton, Feb. 1995.

[9]Sidilkover, D., "Multidimensional Upwinding and Multigrid," AIAA Paper 95–1759, June 1995.

[10]Mohanraj, R., Neumeier, Y., and Zinn, B. T., "Characteristic-Based Treatment of Source Terms in Euler Equations for Roe Scheme," *AIAA J.*, Vol. 37, No. 4, April 1999, pp. 417–424.

[11]Wood, W. A., *Fluctuation Splitting for Aerothermodynamics*, Ph.D. thesis, Va Tech, 2001 (*projected*).

[12]Haselbacher, A. C., McGuirk, J. J., and Page, G. J., "Finite-Volume Discretization Aspects for Viscous Flows on Mixed Unstructured Grids," *AIAA J.*, Vol. 37, No. 2, Feb. 1999, pp. 177–184.

[13]Wood, W. A. and Kleb, W. L., "Diffusion Characteristics of Upwind Schemes on Unstructured Triangulations," AIAA Paper 98–2443, June 1998.

[14]Struijs, R., Deconinck, H., de Palma, P., Roe, P., and Powell, K. G., "Progress on Multidimensional Upwind Euler Solvers for Unstructured Grids," AIAA Paper 91–1550, June 1991.

[15]Gnoffo, P. A., "An Upwind-Biased, Point-Implicit Relaxation Algorithm for Viscous, Compressible Perfect-Gas Flows," NASA TP 2953, February 1990.

[16]Haselbacher, A. C., McGuirk, J. J., and Page, G. J., "Finite-Volume Discretisation Aspects for Viscous Flows on Mixed Unstructured Grids," AIAA Paper 97–1946, June 1997.

[17]Courant, R., Friedrichs, K. O., and Lewy, H., "Über die Partiellen Differenzengleichurgen der Mathematischen Physik," *Mathematische Annalen*, Vol. 100, 1928, pp. 32–74, (see also Ref. 24).

[18]Maccoll, J. W., "The Conical Shock Wave Formed by a Cone Moving at High Speed," *Proceedings of the Royal Society for Aeronautics*, Vol. 159, 1937.

[19]Blasius, H., "The Boundary Layers in Fluids with Little Friction," NACA TM 1256, February 1950.

[20]Kleb, W. L., Wood, W. A., and van Leer, B., "Efficient Multi-Stage Time Marching for Viscous Flows via Local Preconditioning," AIAA Paper 99–3267, June 1999.

[21]Gnoffo, P. A., Gupta, R. N., and Shinn, J. L., "Conservation Equations and Physical Models for Hypersonic Air Flows in Thermal and Chemical Nonequilibrium," NASA TP 2867, Feb. 1989.

[22]Cheatwood, F. M. and Gnoffo, P. A., "User's Manual for the Langley Aerothermodynamic Upwind Relaxation Algorithm (LAURA)," NASA TM 4674, April 1996.

[23]Anderson, W. K. and Bonhaus, D. L., "An Implicit Upwind Algorithm for Computing Turbulent Flows on Unstructured Grids," *Comp. and Fluids*, Vol. 23, No. 1, Jan. 1994, pp. 1–21.

[24]Courant, R., Friedrichs, K. O., and Lewy, H., "On the Partial Difference Equations of Mathematical Physics," *IBM Journal*, Vol. 5, March 1967, pp. 215–234, (also as AEC Research and Development Report NYO-7689).